

Domain Adaptive Diabetic Retinopathy Grading with Model Absence and Flowing Data

Wenxin Su¹, Song Tang^{*1,2}, Xiaofeng Liu³, Xiaojing Yi⁴, Mao Ye⁶,
Chunxiao Zu¹, Jiahao Li⁵, and Xiatian Zhu⁷

¹University of Shanghai for Science and Technology ² Universität Hamburg
³Yale University ⁴ Sichuan Eye Hospital ⁵ Peking Union Medical College Hospital
⁶University of Electronic Science and Technology of China ⁷ University of Surrey

steventangsong@gmail.com

Abstract

Domain shift (the difference between source and target domains) poses a significant challenge in clinical applications, e.g., Diabetic Retinopathy (DR) grading. Despite considering certain clinical requirements, like source data privacy, conventional transfer methods are predominantly model-centered and often struggle to prevent model-targeted attacks. In this paper, we address a challenging **Online Model-aGnostic Domain Adaptation (OMG-DA)** setting, driven by the demands of clinical environments. This setting is characterized by the absence of the model and the flow of target data. To tackle the new challenge, we propose a novel approach, **Generative Unadversarial ExampleS (GUES)**, which enables adaptation from a data-centric perspective. Specifically, we first theoretically reformulate conventional perturbation optimization in a generative way—learning a perturbation generation function with a latent input variable. During model instantiation, we leverage a Variational AutoEncoder to express this function. The encoder with the reparameterization trick predicts the latent input, whilst the decoder is responsible for the generation. Furthermore, the saliency map is selected as pseudo-perturbation labels. Because it not only captures potential lesions but also theoretically provides an upper bound on the function input, enabling the identification of the latent variable. Extensive comparative experiments on DR benchmarks with both frozen pre-trained models and trainable models demonstrate the superiority of GUES, showing robustness even with small batch size.

^{*}Corresponding author

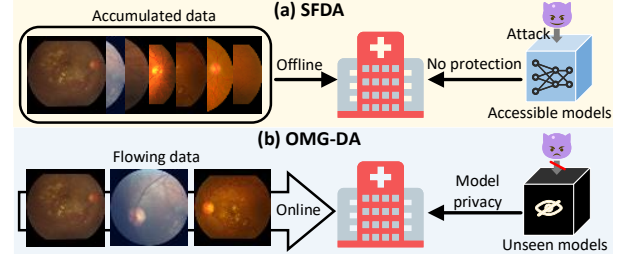


Figure 1. Comparison between the OMG-DA and SFDA settings. (a) In SFDA, adaptation builds upon the accumulated data, which demands significant storage resources in the hospital. Additionally, the models' architecture and parameters are accessible, exposing them to potential attacks. (b) OMG-DA provides a practical scenario: Flowing data mimic the patients' arrival in a stream way, and the models are unseen (strictly controlled) before using them, avoiding attacks like membership inference attacks [26].

1. Introduction

Diabetic Retinopathy (DR) is a significant health concern, ranking among the leading causes of blindness and affecting millions of people worldwide [3]. Early-stage intervention for DR is crucial to preserve vision, highlighting the importance of timely diagnosis [27]. Although deep learning (DL) has demonstrated promising results in automating the grading of DR [6, 8, 37], deploying DL models in real-world clinical settings remains challenging. For example, DL models often struggle to generalize effectively to complex scenarios, such as variations in imaging equipment, ethnic groups, or temporal factors, leading to different data distributions, a challenge known as domain shift [11]. This issue significantly hampers the widespread adoption and success of DL-based diagnostic tools in clinical practice [14].

Recently, many adaptation methods for grading diabetic

Table 1. Comparison between different transfer settings. Notation: source (s), target (t), data \mathbf{x} , label \mathbf{y} , loss function $L(\cdot)$.

Setting name	Model availability	Data flow	Source data privacy	Source data	Target data	Train loss	Test loss
Fine-tuning (FT)	✗	✗	✓	—	$\mathbf{x}_t, \mathbf{y}_t$	$L(\mathbf{x}_t, \mathbf{y}_t)$	—
Domain generalization (DG)	✗	✓	✗	$\mathbf{x}_s, \mathbf{y}_s$	—	$L(\mathbf{x}_s, \mathbf{y}_s)$	—
Unsupervised domain adaptation (UDA)	✗	✓	✗	$\mathbf{x}_s, \mathbf{y}_s$	\mathbf{x}_t	$L(\mathbf{x}_s, \mathbf{y}_s) + L(\mathbf{x}_t)$	—
Source-free domain adaptation (SFDA)	✗	✗	✓	—	\mathbf{x}_t	$L(\mathbf{x}_t)$	—
Test-time adaptation (TTA)	✗	✓	✓	—	\mathbf{x}_t	—	$L(\mathbf{x}_t)$
Online model-agnostic domain adaptation (OMG-DA)	✓	✓	✓	—	\mathbf{x}_t	—	—

retinopathy (DR) have focused on addressing the issue of domain shift [5, 20, 23, 41]. The initial focus on classic transfer learning strategies, including Unsupervised Domain Adaptation (UDA) [20] and Domain Generalization (DG) [4, 5], necessitated the availability of well-annotated source data. Nevertheless, the growing emphasis on privacy protection has shifted research toward the Source-Free Domain Adaptation (SFDA) framework [23, 41]. SFDA involves adapting a source model—pre-trained on the source domain—to the target domain in a self-supervised manner, thereby ensuring the protection of source patient data.

In recent developments, specific needs have emerged in the clinical field. The introduction of model weight-based techniques for reconstructing training data has created a demand for *model privacy* [26, 40], which goes beyond traditional source data protection. In addition, there is a growing requirement for models capable of handling incoming patient data in a flowing fashion, referred to as a *flowing data* constraint [33, 35]. Unfortunately, existing SFDA methods cannot effectively address this challenge, as they rely on full access to the model and require offline training on a pre-collected dataset. Fig. 1 provides an intuitive illustration of this issue.

In this paper, we consider a clinically motivated setting, called **Online Model-agnostic Domain Adaptation (OMG-DA)** and propose a novel **Generative Unadversarial ExampleS (GUES)** approach for the DR grading problem in this new setting. Specifically, OMG-DA presents an extreme safety scenario: The available target data is unlabeled and arrives in a flowing format, with no prior information about the pre-trained source model and data. Tab. 1 provides a detailed comparison with previous adaptation settings.

In GUES, we address the absence of source data and pre-trained models by producing generalized unadversarial examples [24] for unlabeled target data. To this end, we introduce generative unadversarial learning, which theoretically reformulates conventional iterative perturbation optimization. This new method aims to learn a generative function for perturbations and involves addressing two key tasks: (1) Identifying the latent function input, which is the derivative of initial random noise w.r.t. image data, and (2) selecting a self-supervised property to serve as pseudo-perturbation labels. In practice, we leverage a Variational Autoencoder (VAE) [10] based approach to facilitate this learning process.

In terms of function representation, we model the latent input using the encoder along with the reparameterization trick, whilst the decoder accomplishes the generation of individual-perturbation. Additionally, we choose the saliency map as the pseudo-perturbation label for two reasons: (1) It helps discover potential lesions, and (2) it aids in identifying the latent input by providing an upper bound.

Our **contributions** are summarized as follows:

- Pioneering a novel transfer setting OMG-DA, which is closer to real-world clinical scenarios and meets three typical requirements at the same time, including (1) model absence, (2) flowing data, and (3) source data privacy.
- Developing a new OMG-DA approach GUES in the context of DR grading, grounded on the generative unadversarial examples theory, where we learn an individual-perturbation generative function under saliency map supervision, removing relying on labels and models.
- Extensive evaluations on four DR benchmarks, indicating that GUES can largely promote the source model’s performance in the target domain, as well as trainable test-time adaptation models, even at small batch size.

2. Related work

Adaptation methods for DR grading. Driven by real-world medical requirements, domain adaptation has been an attractive topic in this DR grading issue. For instance, Nguyen et al. [20] introduce a UDA approach that enables the model to focus on vessel structures that remain invariant to domain shifts via image reconstruction using labeled source domain data. In SFDA, Zhang et al. [41] propose generating labeled, target-style retinal images to improve the source model’s generalization, relying solely on a pre-trained source model and unlabeled target images. Additionally, DG in DR grading has been explored through domain-invariant feature learning approaches [4] and divergence-based methods [5], leveraging labeled source domain data.

These methods above rely on labeled data, require full access to the model, and necessitate offline training on a pre-collected dataset. In real clinical settings, these requirements can be impractical due to constraints around data and model privacy, as well as the need for real-time adaptability without retraining. In contrast, GUES provides an online adaptation solution that operates without requiring labeled data or access to the model, addressing the domain adaptation problem

in DR grading.

Unadversarial learning. Unadversarial learning was initially developed by Salman et al. [24], aiming to modify input image distribution to make them more easily recognizable by the model. Current mainstreams achieve this learning process by adding class-specific perturbations to the input images. Here, the perturbations are generated based on the gradient of an objective function w.r.t. image. This approach allows for the design of unadversarial examples without model training. For example, based on [24], NSA [25] introduces a method to generate more natural perturbations using a trainable generator. Similarly, CAT [18] demonstrates a new distance metric for generating unadversarial examples.

All existing unadversarial learning methods require access to model parameters, outputs, and labeled data. This dependency invalidates them in our OMG-DA setting which only has access to unlabeled target data. In addition to this, our GUES produces individualized unadversarial examples in a generative manner, which stands out from previous methods that focus on class-specific unadversarial examples.

Saliency map for medical image. A fine-grained saliency map is a pixel feature generated by calculating the central-surround differences within images, identifying salient regions without any need for training [19]. This feature is widely applied in various medical image analysis tasks to extract pathologically important regions [9, 22, 31, 36]. For instance, in DR grading, studies such as [9, 22] utilize saliency maps to guide models in focusing on critical features like the optic disc, cup, and vessel structures. Similarly, in brain tumor detection, Tomar et al. [31] leverage saliency maps to enhance the model’s attention on tumor and bone structures. In skin cancer detection, saliency maps help isolate lesion regions with distinctive features, such as lumpiness, which are essential for accurate diagnosis [36].

As stated above, existing works primarily use saliency maps to highlight lesion regions. Unlike the conventional usage of saliency maps, GUES selects saliency maps as pseudo-perturbation labels.

3. Problem Statement of OMG-DA

Given two different but related domains, *i.e.*, source domain \mathcal{S} and target domain \mathcal{T} , \mathcal{S} contains n_s labeled samples, while \mathcal{T} has n unlabeled data. Both labeled and unlabeled samples share the same C categories. Let \mathcal{X}_s and \mathcal{Y}_s be the source samples and the corresponding labels. Similarly, we denote the target samples and their labels by $\mathcal{X}_t = \{\mathbf{x}_t^i\}_{i=1}^n$ and $\mathcal{Y}_t = \{y_t^i\}_{i=1}^n$, respectively, where n signifies the number of samples. The source model θ_s is pre-trained on $\{\mathcal{X}_s, \mathcal{Y}_s\}$.

OMG-DA is featured in (1) the absence of the source model θ_s and domain \mathcal{S} and (2) the flowing target data \mathcal{X}_t the same as the TTA setting [35]. Unlike previous transfer settings that are model adaptation-centered [15, 29, 30, 39],

OMG-DA considers adaptation from the perspective of data. Specifically, OMG-DA aims to modify the distribution of target data to facilitate downstream tasks.

4. Methodology

4.1. Generative Unadversarial Examples

The part begins with a brief recap of traditional unadversarial learning [24]. Unlike adversarial learning [28] that generates confusing samples to mislead models, unadversarial learning aims to construct generalized samples, tackling promoting out-of-distribution issues. Formally, this learning can be summarized in the following optimization problem.

$$\hat{\delta} = \arg \min_{\delta} L(f_{\theta}(x + \delta), y), s.t. \|\delta\| \leq \epsilon \quad (1)$$

where $L(\cdot)$ denotes objective function, *e.g.*, cross-entropy loss for classification tasks, x and y are input image and its label, f_{θ} is a pre-trained model with parameters θ , δ is a perturbation, ϵ is a small threshold. The current scheme solves this problem in an iterative way formulated as

$$\delta_{k+1} = \delta_k + \alpha \cdot \text{sign}(\nabla_x L(f_{\theta}(x + \delta_k), y)), k \in [0, K - 1], \quad (2)$$

where α is a trade-off parameter, K is iteration number, δ_0 is an initial random noise. In the inference phase, the optimal perturbation $\hat{\delta}$ is integrated into the input x , forming an unadversarial example $\hat{x} = x + \hat{\delta}$, which is easily recognizable by the model f_{θ} . Obviously, the conventional unadversarial paradigm cannot meet our OMG-DA setting due to the absence of f_{θ} , L , and the label y .

In this paper, we re-consider the iterative optimization process above and obtain the theorem below (The proof is provided in Supplementary).

Theorem 1 *Given the unadversarial learning problem defined in Eq. (9), the iterative process featured by Eq. (10) can be expressed as the following generative form.*

$$\delta_k = \delta_0 + V \cdot F_{\Phi} \left(\frac{\partial \delta_0}{\partial x} \right), \quad (3)$$

where δ_0 is an initial random noise, $V > 0$ is a bound constant, F_{Φ} is a generative function, $\frac{\partial \delta_0}{\partial x}$ is a latent variable.

Grounded on Theorem 1, we have: When δ_k converges to optimal $\hat{\delta}$, *i.e.*, $\delta_k \rightarrow \hat{\delta}$, function F_{Φ} also evolves to the optimal one, denoted by \hat{F}_{Φ} , *i.e.*, $F_{\Phi} \rightarrow \hat{F}_{\Phi}$. This provides an insight: *The unadversarial learning problem above can also be solved in a generative fashion.* Correspondingly, the generated data are termed generative unadversarial examples.

4.2. Model Instantiation

Within this context of generative unadversarial learning, conventional unadversarial learning presented in Eq. (9) is

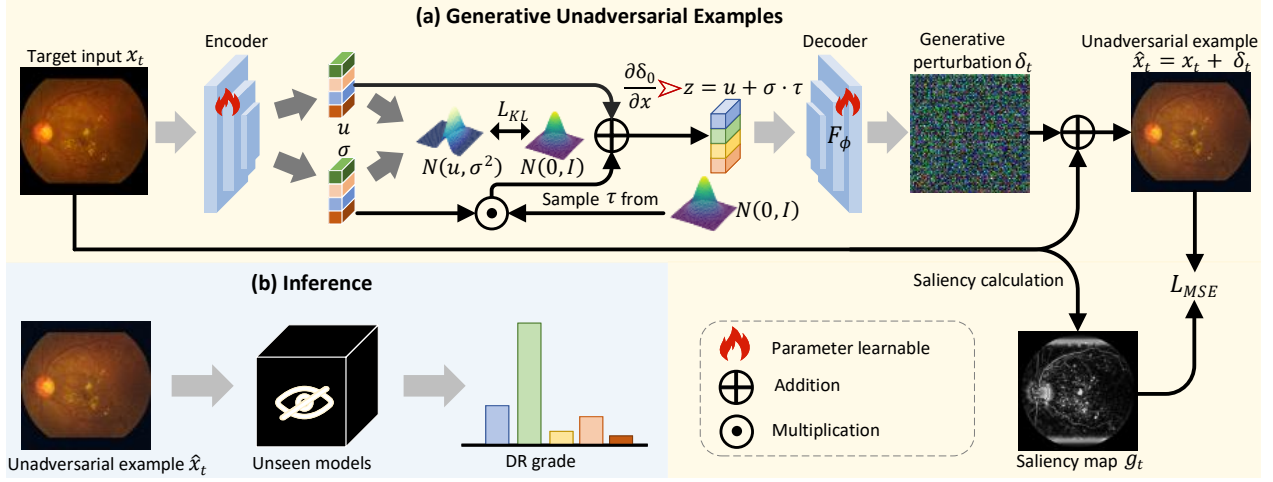


Figure 2. The instantiation framework of GUES in the OMG-DA setting. (a) For target input x_t , the VAE model generates individual perturbation $\delta_t = F_\Phi \left(\frac{\partial \delta_0}{\partial x} \right)$. After that, the by-pass path incorporates δ_t and x_t to create the generative unadversarial example \hat{x}_t . Treating x_t 's saliency map g_t as reconstruction supervision for model training. (b) At the inference phase, the generated unadversarial example \hat{x}_t is directly provided to the frozen source model or other trainable models.

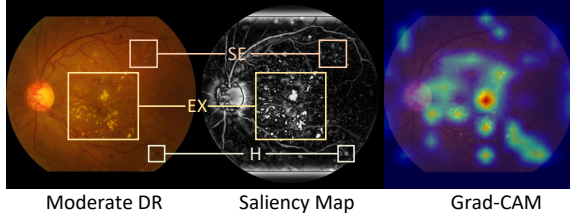


Figure 3. Explanation in choosing fine-grained saliency maps as supervision. **Left:** The testing fundus image selected from “Moderate DR” class in APTOS demonstrates that H (hemorrhages), SE (soft exudates), and EX (hard exudates) are essential characteristics to judge the DR grade. **Middle:** The saliency map highlights those lesions. **Right:** The gradient-CAM visualization of the source model on task DDR \rightarrow APTOS.

boiled down to learning $F_\Phi \left(\frac{\partial \delta_0}{\partial x} \right)$. We can achieve this by training a generative neural network. To make this solution sense, we have to solve two difficulties as follows. **(A)** One is the identification of $\frac{\partial \delta_0}{\partial x}$ when the relationship between them is unknown. **(B)** The other is selecting property supervision (pseudo-perturbation labels) to drive $\delta_k \rightarrow \hat{\delta}$.

Solution to problem A. In practice, considering derivative $\frac{\partial \delta_0}{\partial x}$ is relevant with both random noise δ_0 and input image x , we sample it from a certain Gaussian distribution associated with x . Furthermore, the output size of F_Φ is the same as x . Therefore, we employ the VAE model to jointly model $\frac{\partial \delta_0}{\partial x}$ and F_Φ , since VAE is an autoencoder characterized by random sampling. Specifically, as shown in Fig.2 (a), we approximate $\frac{\partial \delta_0}{\partial x}$ by latent variable z , which is jointly determined by input x and sampled random signal τ . As for

F_Φ , it is demonstrated by the decoder module. Suppose $D(\cdot)$ is the decoder, $E_\tau(\cdot)$ is the encoder with reparameterization trick, our scheme can be formulated as

$$D(E_\tau(x)) \rightarrow F_\Phi \left(\frac{\partial \delta_0}{\partial x} \right), E_\tau(x) \rightarrow \frac{\partial \delta_0}{\partial x}, D(\cdot) \rightarrow F_\Phi(\cdot). \quad (4)$$

Solution to problem B. We adopt the fine-grained saliency map as the supervision. Two reasons contribute to our selection. First of all, the empirical results show that, for the specific task of DR grading, the saliency map is an acceptable pseudo-perturbation. Specifically, perturbation in the unadversarial context enhances the regions associated with the category and reduces the prominence of other areas, thereby identifying the lesion zones relevant to DR grading. As illustrated in Fig. 3, the saliency map effectively identifies potential lesions, such as hemorrhages, soft exudates, and hard exudates. Furthermore, it includes gradient information, as it highlights regions similar to Grad-CAM (Right side). More importantly, we have the theorem below. (The proof is provided in Supplementary)

Theorem 2 Given the partial derivatives of the initial random noise δ_0 w.r.t image x is $\frac{\partial \delta_0}{\partial x}$ and x 's saliency map is $s = G(x)$ where $G(\cdot)$ is the computation function of the saliency map. We have the following relationship:

$$\frac{\partial \delta_0}{\partial x} \leq U \cdot s, \quad (5)$$

where $U > 0$ is a bound constant.

Theorem 2 suggests that the saliency map provides upper bounds for $\frac{\partial \delta_0}{\partial x}$. Namely, s provides relaxed descriptions for the variation $\frac{\partial \delta_0}{\partial x}$. This can help guide the learning of $\frac{\partial \delta_0}{\partial x}$.

GUES framework. Based on the analysis above, we instantiate GUES as the framework depicted in Fig. 2. As shown in sub-figure (a), our method integrates a VAE model and by-pass connection, achieving the learning of $F_\Phi(\frac{\partial\delta_0}{\partial x})$. Specifically, $\frac{\partial\delta_0}{\partial x}$ is sampled from an input x_t -featured Gaussian distribution $N(\mu, \sigma)$, which is jointly learned using the encoder and reparameterization. The decoder, representing F_Φ , then transforms $\frac{\partial\delta_0}{\partial x}$ into a generative perturbation δ_t . Finally, the by-pass structure incorporates x_t and δ_t to produce \hat{x}_t . During the inference phase, as shown in Fig. 2 (b), for a specific testing sample, the trained GUES model outputs the corresponding generative unadversarial examples to the frozen or fine-tuning model that early unseen.

Loss function The loss function for GUES training consists of two components. First, we enforce the latent space with mean μ and variance σ satisfy the standard normal distribution $\mathcal{N}(0, I)$. Suppose the encoder in VAE models the posterior distribution $q(z|x_t) = \mathcal{N}(\mu(x_t), \sigma^2(x_t))$, this regularization can be formulated as:

$$L_{KL} = D_{KL}(q(z|x_t) \parallel \mathcal{N}(0, I)), \quad (6)$$

where function D_{KL} computes the Kullback-Leibler divergence. The other reconstruction loss between the unadversarial example \hat{x}_t and saliency map g_t is presented by the following regression form:

$$L_{MSE} = \|\hat{x}_t - g_t\|_2. \quad (7)$$

Formally, combining Eq. (6) and Eq. (7), the final objective of GUES can be summarized as:

$$L_{GUES} = \alpha L_{KL} + \beta L_{MSE}, \quad (8)$$

where α and β are trade-off parameters. For clarity, we summarize the training procedure of GUES in Algorithm 1.

In Eq. (8), the first item L_{KL} ensures the learning of $\frac{\partial\delta_0}{\partial x}$. On the one hand, as aforementioned, we use z to present $\frac{\partial\delta_0}{\partial x}$. L_{KL} aligns the z space with $\mathcal{N}(0, I)$, thereby linking the random noise to $\frac{\partial\delta_0}{\partial x}$. On the other hand, $q(z|x_t)$ in L_{KL} is a function of input x_t , building relationship x_t to $\frac{\partial\delta_0}{\partial x}$. Additionally, the reconstruction regulated by the second item L_{MSE} encourage $\delta_k \rightarrow \hat{\delta}$.

5. Experiments

5.1. Datasets

We perform evaluation experiments on four existing fundus benchmarks, including **APTOS** [1], **DDR** [13], **DeepDR** [17], and **Messidor-2** (termed MD2) [7]. Those datasets share five grading/classes: no DR, mild DR, moderate DR, severe DR, and proliferative DR. Taking each dataset as a separate domain, we form 12 transfer tasks crossing domains. For example, as APTOS is the source domain while

Algorithm 1 The pipeline of proposed GUES

Input: Online batch samples \mathcal{B} , a trainable VAE θ_v consists of an encoder $E_\tau(\cdot)$ with the reparameterization trick and a decoder $D(\cdot)$.

Procedure:

- 1: **for** x_i in \mathcal{B} **do**
 - 2: Approximate the latent function input by $E_\tau(x_i)$;
 - 3: Learn a generative function for perturbation δ_i by D ;
 - 4: Calculate individual perturbations δ_i by $D(E_\tau(x))$;
 - 5: Create the unadversarial example \hat{x}_i by incorporating δ_i and x_i through the bypass path.
 - 6: Generate a fine-grained saliency map g_i of the x_i ;
 - 7: Update θ_v with Eq.(8), taking g_t as a supervision.
 - 8: **end for**
 - 9: **return** The generative unadversarial examples \hat{x}
-

the others are target domains, we have three transfer tasks APTOS→DDR, APTOS→DeepDR, and APTOS→MD2. The illustration of the label distribution and the domain shift of the four datasets is demonstrated in Supplementary.

It should be **noted that** all datasets have a severe class imbalance (e.g., “no DR” class itself takes up to 45.8% of the DDR dataset).

5.2. Implementation Detail

Source model pre-training. We adopt the DeiT-base network [32] as the backbone of the source pre-trained model, training it in a supervised manner using the source data and corresponding ground truths. During this source training phase, the adopted objective is the classic cross-entropy loss with label smoothing, the same as other methods [15, 38, 39].

Variational autoencoder setting. The VAE model is an eight-layer convolutional architecture with a latent space dimension of 10. We do not employ a pre-trained VAE and utilize a VAE without fine-tuning on any other dataset, ensuring that the learning component $F_\Phi(\frac{\partial\delta_0}{\partial x})$ are unbiased and independent of prior pre-training data.

Parameter setting. For the trade-off parameters in Eq. (8), we set α to 1.0, while β is tuned with $\{0.0001, 0.01, 1\}$ to ensure that the loss values of L_{KL} and L_{MSE} remain on the same scale.

Training setting. We adopt the batch size of 64, SGD optimizer with a momentum of 0.9 and a learning rate of 1e-5 on all datasets. All experiments are conducted with PyTorch on a single GPU of RTX A6000.

5.3. Comparison Settings

Evaluation metrics. To account for unbalanced datasets, in addition to conventional classification accuracy (termed ACC), we adopt the measure of Quadratic Weighted Kappa (termed QWK) [2] and the average of QWK and ACC

Table 2. The results of Source, SFDA, TTA, OMG-DA, and OMG-DA combination methods on datasets APTOS, DeepDR, DDR, and MD2 are presented. The improvements over baseline methods Source, SHOT-IM, and TENT are highlighted as (+x.x).

Method	Venue	APTOS→DDR			APTOS→DeepDR			APTOS→MD2			DDR→APTOS			DDR→DeepDR			DDR→MD2			DeepDR→APTOS		
		ACC	QWK	AVG	ACC	QWK	AVG	ACC	QWK	AVG	ACC	QWK	AVG	ACC	QWK	AVG	ACC	QWK	AVG	ACC	QWK	AVG
Source	–	60.6	59.2	59.9	52.6	71.7	62.1	60.9	48.7	54.8	65.6	72.9	69.3	45.0	60.6	52.8	49.4	34.6	42.0	43.4	71.6	57.5
GUES	–	62.0	59.5	60.8	53.0	69.7	61.3	59.8	46.7	53.3	76.0	81.8	78.9	56.4	68.7	62.5	59.1	47.6	53.3	46.5	74.1	60.3
SHOT [15]	ICML20	66.9	69.0	67.9	53.6	73.5	63.6	51.7	38.0	44.8	77.0	84.2	80.6	59.2	74.6	66.9	57.1	43.1	50.1	62.3	82.5	72.4
NRC [39]	NeurIPS21	61.9	65.2	63.5	51.6	70.9	61.3	54.1	40.3	47.2	60.3	76.3	68.3	52.0	69.1	60.5	50.6	35.2	42.9	52.0	74.3	63.2
CoWA [12]	ICML22	59.0	64.9	62.0	51.0	70.7	60.8	53.0	37.3	45.1	57.2	74.5	65.8	50.1	66.8	58.4	53.1	39.6	46.3	50.4	73.0	61.7
PLUE [16]	CVPR23	62.0	65.1	63.6	51.3	69.7	60.5	54.5	41.1	47.8	63.4	64.2	63.8	54.3	64.8	59.5	51.6	28.2	39.9	54.6	70.5	62.6
TPDS [29]	IJCV24	66.6	67.8	67.2	51.6	71.5	61.5	52.7	40.7	46.7	76.6	83.9	80.2	58.0	73.1	65.6	54.5	41.0	47.8	60.8	80.0	70.4
SHOT-IM [15]	ICML20	66.5	69.2	67.9	52.6	73.6	63.1	53.2	36.6	44.9	75.9	82.1	79.0	58.5	73.9	66.2	57.3	43.5	50.4	61.9	84.0	72.9
TENT [35]	ICLR20	59.9	50.2	55.1	53.1	70.1	61.6	61.4	48.4	54.9	75.2	82.4	78.8	55.1	68.4	61.7	60.8	50.5	55.6	60.2	79.7	69.9
SAR [21]	ICLR23	67.9	63.8	65.8	53.6	73.0	63.3	57.2	44.9	51.1	75.6	83.5	79.5	55.6	71.6	63.6	49.2	37.0	43.1	59.5	79.3	69.4
GUES+SHOT-IM –	–	68.6	68.5	68.5	53.5	72.8	63.2	55.7	43.8	49.7	77.2	83.1	80.2	60.5	75.1	67.8	61.5	51.2	56.3	62.6	83.2	72.9
GUES+TENT –	–	61.8	56.3	59.0	53.2	70.0	61.6	61.1	47.2	54.1	75.9	83.0	79.4	58.7	70.8	64.7	63.3	53.8	58.6	54.9	77.6	66.3

Method	Venue	DeepDR→DDR			DeepDR→MD2			MD2→APTOS			MD2→DDR			MD2→DeepDR			ACC	Avg. QWK	AVG
		ACC	QWK	AVG	ACC	QWK	AVG	ACC	QWK	AVG	ACC	QWK	AVG	ACC	QWK	AVG			
Source	–	56.4	66.9	61.7	48.7	50.2	49.4	43.9	70.3	57.1	60.2	56.5	58.3	59.8	58.4	59.1	53.9	60.1	57.0
GUES	–	57.3	65.6	61.4	48.3	52.0	50.1	59.3	76.2	67.7	64.7	55.8	60.2	58.6	57.1	57.8	58.4 (+4.5)	62.9 (+2.8)	60.7 (+3.7)
SHOT [15]	ICML20	57.4	71.2	64.3	48.8	41.5	45.2	52.7	73.0	62.8	54.6	59.2	56.9	59.6	70.2	64.9	58.4	65.0	61.7
NRC [39]	NeurIPS21	44.9	60.9	52.9	49.8	41.8	45.8	48.8	69.1	58.9	52.8	52.8	52.8	58.0	62.8	60.4	53.1	59.9	56.5
CoWA [12]	ICML22	48.7	58.4	53.6	49.9	42.7	46.3	51.0	70.1	60.5	49.6	50.9	50.3	57.6	60.6	59.1	56.9	61.9	59.4
PLUE [16]	CVPR23	47.2	53.5	50.4	56.4	47.4	51.9	56.0	69.1	62.6	56.5	54.3	55.4	58.8	64.8	61.8	55.5	57.7	56.6
TPDS [29]	IJCV24	59.3	69.4	64.3	50.5	42.4	46.4	60.3	74.9	67.6	60.0	60.4	60.2	58.9	63.0	60.9	59.2	64.0	61.6
SHOT-IM [15]	ICML20	54.6	69.4	62.0	51.2	38.2	44.7	61.6	77.9	69.7	57.0	58.7	57.9	57.5	69.8	63.7	59.0	64.7	61.9
TENT [35]	ICLR20	58.5	45.4	51.9	58.3	56.5	57.4	55.1	74.1	64.6	55.8	31.7	43.7	58.0	53.6	55.8	59.3	59.2	59.3
SAR [21]	ICLR23	53.0	66.3	59.6	42.6	33.1	37.9	55.2	73.0	64.1	49.7	48.3	49.0	56.7	65.8	61.3	56.3	61.6	59.0
GUES+SHOT-IM –	–	62.3	71.5	66.9	52.8	47.8	50.3	62.8	78.1	70.4	66.0	59.4	62.7	60.6	68.6	64.6	62.0 (+3.0)	66.9 (+2.2)	64.5 (+2.6)
GUES+TENT –	–	62.6	61.4	62.0	59.1	57.4	58.2	59.3	75.6	67.5	64.0	50.5	57.2	58.3	56.0	57.1	61.0 (+1.7)	63.3 (+4.1)	62.2 (+2.9)

(termed AVG). The computation rules of them are provided in Supplementary.

Competitors. We compare GUES with nine existing state-of-the-art adaptation methods divided into three groups. (1) *The first group* involves applying the source model directly to the target domain. (2) *The second group* includes five SFDA methods SHOT [15], NRC [39], CoWA [12], PLUE [16], and TPDS [29]. (3) *The third group* comprises three typical TTA methods: SHOT-IM [15], TENT [35], and SAR [21].

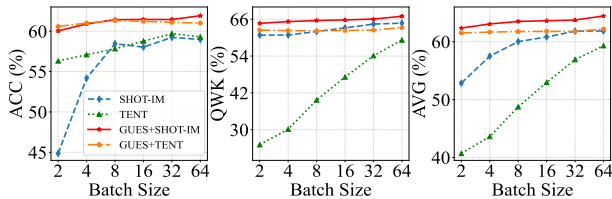


Figure 4. Comparison results with batch size varying from 2 to 64 over the 12 tasks (The details are provided in Supplementary.). **Left, middle, and right** report ACC, QWK, and AVG, respectively.

Comparison protocol in OMG-DA setting. For a comprehensive comparison, our comparison follows two different fashions as follows.

- Case without training: We first generate the unadversarial

examples for the target domain by the trained GUES model and then provide them to the frozen source model.

- Case with training: We plug GUES into other TTA methods (they are also online methods with flowing data) as online image pre-processing.

The two cases evaluate GUES from different aspects. The first isolates the generalization ability of the unadversarial examples generated by GUES, whilst the second highlights GUES’s compatibility with other trainable online schemes.

Corresponding to the comparison protocols above, besides the version GUES corresponding to the case without training, we also introduce GUES+SHOT-IM and GUES+TENT which correspond to the case with training.

5.4. Comparison Results

In this part, we present the comparison results following the cases mentioned above. Also, considering batch size a crucial factor for TTA methods, the results as the batch size varies is provided.

Results without training. The comparisons are shown in Tab. 2. On average, across the 12 tasks and without training of the source model, GUES achieves improvements of **4.5%** in ACC, **2.8%** in QWK, and **3.7%** in AVG compared to the source model. These results demonstrate that GUES modifies the target data distribution effectively, adapting the

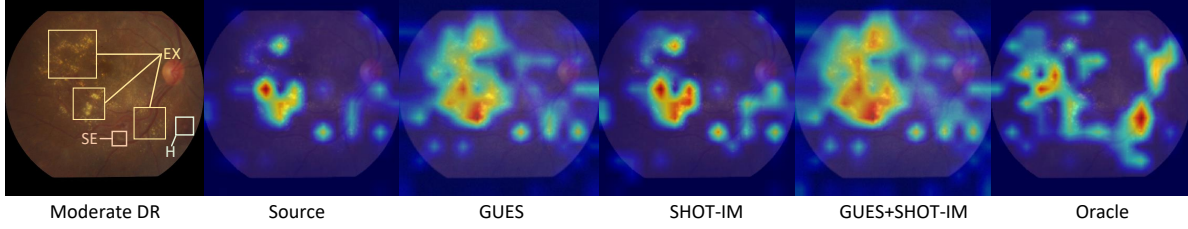


Figure 5. Interpretability analysis based on a typical fundus image from “Moderate DR” class in APTOS. Here, H (hemorrhages), SE (soft exudates), and EX (hard exudates) are essential characteristics to judge the DR grade. The gradient CAM-based heatmap of five models visualizes the capture of those lesions. All models are trained on task $\text{DDR} \rightarrow \text{APTOS}$, where Oracle is trained using ground truth in APTOS.

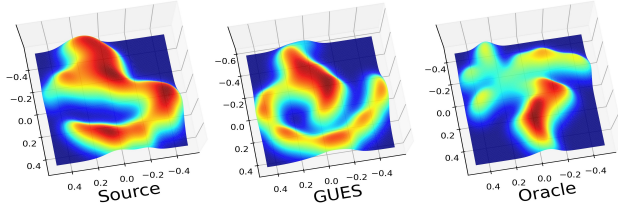


Figure 6. Feature distribution comparison of 3D density charts on task $\text{DDR} \rightarrow \text{APTOS}$. Oracle is trained on APTOS by ground truth.

target domain to align with the source domain.

Results with training. As shown in Tab. 2, GUES+SHOT-IM outperforms the previous best SFDA and TTA methods, respectively surpassing TENT in ACC by **2.7%**, SHOT in QWK by **1.9%**, and SHOT-IM in AVG by **2.6%** on average. Meanwhile, compared to SHOT-IM, GUES+SHOT-IM gains over **3.0%** in ACC, **2.2%** in QWK, and **2.6%** in AVG. Similarly, GUES+TENT improves over TENT by **1.7%** in ACC, **4.1%** in QWK, and **2.9%** in AVG. These results highlight the effectiveness of combining GUES with other methods that require training.

Results with varying batch size. This part isolates the effect of batch size, which is a crucial factor for TTA methods. Fig. 4 depicts the performance variation as batch size varying from 2 to 64 over the 12 tasks. It is observed that TTA methods SHOT-IM and TENT suffer from severe performance drops when the batch size becomes small. SHOT-IM exhibits a decrease of approximately **16%** in ACC when the batch size is reduced from 64 to 2, whilst TENT shows a substantial decline of around **34%** in QWK. Oppose to it, the methods with GUES, SHOT-IM+GUES, and TENT+GUES, do not have evident performance decline at the smaller batch size. Moreover, this combination not only mitigates the drop but also shows improvements when the batch size is 64. This indicates that GUES effectively stabilizes the performance of SHOT-IM and TENT, enhancing their robustness to variations in batch size while boosting their overall effectiveness.

We attribute GUES’s excellent robustness to its ability to predict individual perturbations (see Supplementary for more details on the visualization of perturbations) that focus

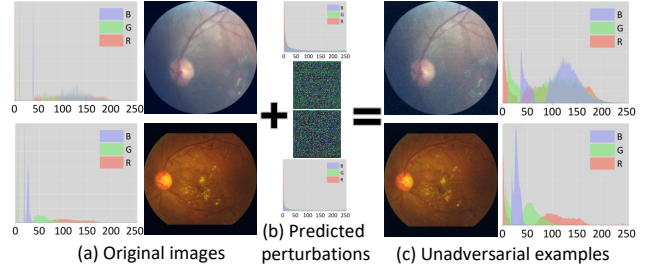


Figure 7. Unadversarial examples visualization of two typical target samples from APTOS. The generative perturbations are generated by the GUES model trained on task $\text{DDR} \rightarrow \text{APTOS}$.

on single image-specific features rather than global data commonalities. For instance, the conventional unadversarial examples approach refines the class-specific perturbation sensitive to batch size. Furthermore, both SHOT-IM and TENT are entropy-based methods that require large-scale batch size for accurate entropy estimation.

5.5. Visualization Analysis

Interpretability. For a better understanding, Fig. 5 demonstrates whether GUES can help capture pathologically relevant features, such as H (hemorrhages), SE (soft exudates), and EX (hard exudates), determining DR grade. First of all, when comparing the source model with GUES, the source model only captures a limited area of the lesion, while GUES effectively captures most of the DR-related features. Furthermore, combining GUES with SHOT-IM (i.e., GUES+SHOT-IM) expands the focus on DR-related features beyond those captured by SHOT-IM alone. Additionally, when comparing the four models to Oracle, only GUES and GUES+SHOT-IM resemble Oracle, suggesting that GUES effectively directs the model’s attention to DR-critical features.

Feature distribution. Taking the task $\text{DDR} \rightarrow \text{APTOS}$ as a toy experiment, we visualize the feature distribution extracted from the final convolutional layer of the prediction model using a 3D density chart. Considering that APTOS is a class-imbalanced dataset, with the “No DR” class alone comprising up to **49.2%** of the dataset, our analysis focuses

Table 3. ACC results of ablation study (%).

#	L_{KL}	L_{MSE}	APTOS	DDR	DeepDR	MD2	Avg.
1	✗	✗	51.0	59.1	52.5	53.0	53.9
2	✓	✗	54.7	58.3	54.9	53.3	55.3
3	✗	✓	56.9	60.1	52.9	52.9	55.7
4	✓	✓	60.6	61.3	56.0	55.7	58.4
5	GUES w/ AE		53.8	60.2	53.8	53.2	55.3
6	GUES w/ Mixup		56.8	60.2	53.0	52.8	55.7
7	GUES w/ Self		56.5	60.4	53.7	54.4	56.3
8	GUES w/ Sal		46.1	34.3	41.8	45.9	42.0

on this crucial property. As shown in Fig. 6, the feature distribution of the source model does not reflect this imbalanced characteristic; instead, it displays a more uniform classification. Conversely, the feature distribution of GUES exhibits a distinct imbalance, with one expanded high-density region alongside several smaller high-density regions, resembling the distribution pattern seen in Oracle.

Visualization of unadversarial examples. This part visualizes unadversarial examples of two typical target samples from APTOS and corresponding generative perturbations, based on the task DDR→APTOS. Considering the generative perturbations alter the original images that may not be easily visible to the naked eye, we collect RGB statistics to illustrate these changes quantitatively. It is observed that in Fig. 7, each channel (R, G, and B) exhibits notable fluctuations, with the RGB statistics of the original images (a) differing significantly from those of the unadversarial examples (c). Additionally, each generative perturbation is unique, meaning that the alterations introduced by these perturbations are individual. These results suggest that the perturbations may help highlight critical DR-related features, refining the model’s focus on diagnostically relevant areas.

5.6. Further Analysis

Ablation study. In this part, we evaluate the effect of objective loss, as well as the components involved in GUES including the sampling strategy and saliency map-based supervision. To address the first issue, we conduct a progressive experiment. The top four rows of Tab. 3 list the ablation results where the source model’s performance is the baseline. Using L_{KL} or L_{MSE} alone yields an average ACC improvement of approximately **1.4%** and **1.8%**, respectively, over the baseline. As both of them work, the ACC increases **3.5%** on average further. The results indicate that all objective components positively affect the final performance.

To evaluate the impact of the sampling component, we propose a variation method of GUES, GUES w/ AE, where we remove this sampling process by replacing VAE with a conventional Auto-encoder model. In addition, two GUES variations are used to assess the advantage of saliency map-based supervision. Specifically, GUES w/ Mixup replaces the saliency maps with a Mixup of saliency maps and origi-

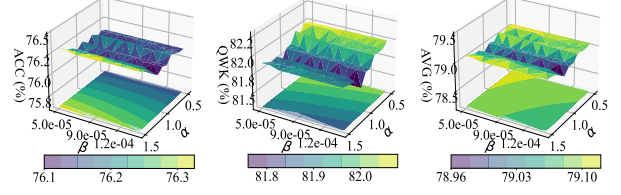


Figure 8. Parameter sensitiveness study results over $\alpha \times \beta$ based on task DDR→APTOS. From left to right, there are results on ACC, QWK, and AVG, respectively.

nal images, whilst GUES w/ Self replaces the saliency maps with the original images. As presented in the Tab. 3, compared with the full version of GUES (the fourth row), GUES w/ AE, GUES w/ Mixup and GUES w/ Self decrease by **3.1%** at least on average. Besides, replacing the original images with saliency maps as inputs (GUES w/ Sal) leads to a significant drop of about **15.4%**. Above these experiments confirm the effectiveness of our design choices.

Parameter sensitiveness. Taking the task DDR→APTOS as a toy experiment, we present the GUES performance varying as hyper-parameters $0.5 \leq \alpha \leq 1.5$ with 0.1 steps, $0.00005 \leq \beta \leq 0.00014$ with 0.00001 steps. As depicted in Fig. 8, the ACC, QWK, and AVG variation surfaces show fluctuations in the tiny performance zone, with approximately **0.2%** in ACC, **0.25%** in QWK, and **0.4%** in AVG. This observation suggests that GUES is insensitive to alterations in α and β .

Limitation. GUES uses the saliency map to guide the learning of the generative function. This method is effective for DR grading but encounters challenges in natural image scenarios. The natural images contain rich semantics, such as shape, relative structure, and complex background, which are not all relevant to tasks. However, the saliency map blindly highlights all those factors, struggling to capture the task-specific ones. In a theoretical point-view, the richness of these semantics means significant variations, resulting in a super-relaxed bound constant U (see Theorem 2) that undermines the descriptive power of the saliency map for $\frac{\partial \delta_0}{\partial x}$. In contrast, fundus images are more monolithic, implying a smaller U that justifies the usage of the saliency map. (The further discussion is provided in Supplementary)

6. Conclusion

In this paper, we propose a clinically motivated setting, OMG-DA, where the models are unseen prior to their use, and only target data flows are accessible. This setting ensures both model protection and source data privacy in a data flow scenario. To adapt to the target domain without access to the models, we introduce a GUES approach. Instead of conventional iterative optimization, we generate unadversarial examples for flowing target data by directly predicting

individual perturbations. This approach is grounded in the theoretical results of generative unadversarial learning. In practice, we utilize the VAE model to learn the perturbation generation function with a latent input variable. Furthermore, we demonstrate that saliency maps can serve as an upper bound for this latent variable. This relationship inspires us to use the saliency maps as pseudo-perturbation labels for model training. Extensive experiments conducted on four DR benchmarks confirm that the proposed method can achieve state-of-the-art results, when it pairs with both frozen pre-trained and fine-tuning models.

References

- [1] Aptos: Aptos 2019 blindness detection website. <https://www.kaggle.com/c/aptos2019-blindness-detection>, accessed February 20, 2022. 5, 13
- [2] Quadratic weighted kappa. <https://www.Eyepacs.com/aroraaman/quadratic-kappa-metric-explained-in-5-simple-steps>, accessed July 2022. 5
- [3] Eman AbdelMaksoud, Sherif Barakat, and Mohammed El-mogy. A comprehensive diagnosis system for early signs and different diabetic retinopathy grades using fundus retinal images based on pathological changes detection. *Computers in Biology and Medicine*, 126:104039, 2020. 1
- [4] Mohammad Atwany and Mohammad Yaqub. Drgen: domain generalization in diabetic retinopathy classification. In *MICCAI*, 2022. 2
- [5] Haoxuan Che, Yuhan Cheng, Haibo Jin, and Hao Chen. Towards generalizable diabetic retinopathy grading in unseen domains. In *MICCAI*, 2023. 2
- [6] Ling Dai, Liang Wu, Huating Li, Chun Cai, Qiang Wu, Hongyu Kong, Ruhan Liu, Xiangning Wang, Xuhong Hou, Yuexing Liu, et al. A deep learning system for detecting diabetic retinopathy across the disease spectrum. *Nature communications*, 12(1):3242, 2021. 1
- [7] Etienne Decencière, Xiwei Zhang, Guy Cazuguel, Bruno Lay, Béatrice Cochener, Caroline Trone, Philippe Gain, John-Richard Ordóñez-Varela, Pascale Massin, Ali Erginay, et al. Feedback on a publicly distributed image database: the mesidor database. *Image Analysis & Stereology*, pages 231–234, 2014. 5, 13
- [8] Along He, Tao Li, Ning Li, Kai Wang, and Huazhu Fu. Cabnet: Category attention block for imbalanced diabetic retinopathy grading. *IEEE Transactions on Medical Imaging*, 40(1):143–153, 2020. 1
- [9] Yijin Huang, Junyan Lyu, Pujin Cheng, Roger Tam, and Xiaoying Tang. Ssit: Saliency-guided self-supervised image transformer for diabetic retinopathy grading. *IEEE Journal of Biomedical and Health Informatics*, 2024. 3
- [10] Diederik P Kingma. Auto-encoding variational bayes. *arXiv:1312.6114*, 2013. 2
- [11] Wouter M Kouw and Marco Loog. An introduction to domain adaptation and transfer learning. *arXiv:1812.11806*, 2018. 1
- [12] Jonghyun Lee, Dahuin Jung, Junho Yim, and Sungroh Yoon. Confidence score for source-free unsupervised domain adaptation. In *ICML*, 2022. 6
- [13] Tao Li, Yingqi Gao, Kai Wang, Song Guo, Hanruo Liu, and Hong Kang. Diagnostic assessment of deep learning algorithms for diabetic retinopathy screening. *Information Sciences*, 501:511–522, 2019. 5, 13
- [14] Tao Li, Wang Bo, Chunyu Hu, Hong Kang, Hanruo Liu, Kai Wang, and Huazhu Fu. Applications of deep learning in fundus images: A review. *Medical Image Analysis*, 69:101971, 2021. 1
- [15] Jian Liang, Dapeng Hu, and Jiashi Feng. Do we really need to access the source data? source hypothesis transfer for unsupervised domain adaptation. In *ICML*, 2020. 3, 5, 6, 14
- [16] Mattia Litrico, Alessio Del Bue, and Pietro Morerio. Guiding pseudo-labels with uncertainty estimation for source-free unsupervised domain adaptation. In *CVPR*, 2023. 6
- [17] Ruhan Liu, Xiangning Wang, Qiang Wu, Ling Dai, Xi Fang, Tao Yan, Jaemin Son, Shiqi Tang, Jiang Li, Zijian Gao, et al. Deepdrid: Diabetic retinopathy—grading and image quality estimation challenge. *Patterns*, 3(6), 2022. 5, 13
- [18] Xingbin Liu, Huafeng Kuang, Xianming Lin, Yongjian Wu, and Rongrong Ji. Cat: Collaborative adversarial training. *arXiv:2303.14922*, 2023. 3
- [19] Sebastian Montabone and Alvaro Soto. Human detection using a mobile platform and novel features derived from a visual saliency mechanism. *Image and Vision Computing*, 28(3):391–402, 2010. 3
- [20] Duy MH Nguyen, Truong TN Mai, Ngoc TT Than, Alexander Prange, and Daniel Sonntag. Self-supervised domain adaptation for diabetic retinopathy grading using vessel image reconstruction. In *KI*, 2021. 2
- [21] Shuaicheng Niu, Jiaxiang Wu, Yifan Zhang, Zhiquan Wen, Yaofo Chen, Peilin Zhao, and Mingkui Tan. Towards stable test-time adaptation in dynamic wild world. In *ICLR*, 2023. 6
- [22] Jiaming Qiu, Weikai Huang, Yijin Huang, Nanxi Yu, and Xiaoying Tang. Augpaste: A one-shot approach for diabetic retinopathy detection. *Biomedical Signal Processing and Control*, 96:106489, 2024. 3
- [23] Jinye Ran, Guanghua Zhang, Fan Xia, Ximei Zhang, Juan Xie, and Hao Zhang. Source-free active domain adaptation for diabetic retinopathy grading based on ultra-wide-field fundus images. *Computers in Biology and Medicine*, 174:108418, 2024. 2
- [24] Hadi Salman, Andrew Ilyas, Logan Engstrom, Sai Vemprala, Aleksander Madry, and Ashish Kapoor. Unadversarial examples: Designing objects for robust vision. In *NeurIPS*, 2021. 2, 3
- [25] Abhijith Sharma, Phil Munz, and Apurva Narayan. Nsa: Naturalistic support artifact to boost network confidence. In *IJCNN*, 2023. 3
- [26] Reza Shokri, Marco Stronati, Congzheng Song, and Vitaly Shmatikov. Membership inference attacks against machine learning models. In *S&P*, 2017. 1, 2
- [27] Daniel E Singer, David M Nathan, Howard A Fogel, and Andrew P Schachar. Screening for diabetic retinopathy. *Annals of Internal Medicine*, 116(8):660–671, 1992. 1
- [28] C Szegedy. Intriguing properties of neural networks. *arXiv:1312.6199*, 2013. 3

- [29] Song Tang, An Chang, Fabian Zhang, Xiatian Zhu, Mao Ye, and Changshui Zhang. Source-free domain adaptation via target prediction distribution searching. *International Journal of Computer Vision*, 132(3):654–672, 2024. [3](#), [6](#)
- [30] Song Tang, Wenxin Su, Mao Ye, Jianwei Zhang, and Xiatian Zhu. Unified source-free domain adaptation. *arXiv:2403.07601*, 2024. [3](#)
- [31] Nishtha Tomar, Sushmita Chandel, and Gaurav Bhatnagar. A visual attention-based algorithm for brain tumor detection using an on-center saliency map and a superpixel-based framework. *Healthcare Analytics*, 5:100323, 2024. [3](#)
- [32] Hugo Touvron, Matthieu Cord, Matthijs Douze, Francisco Massa, Alexandre Sablayrolles, and Hervé Jégou. Training data-efficient image transformers & distillation through attention. In *ICML*, 2021. [5](#)
- [33] Jeya Maria Jose Valanarasu, Pengfei Guo, VS Vibashan, and Vishal M Patel. On-the-fly test-time adaptation for medical image segmentation. In *MIDL*, 2024. [2](#)
- [34] Hemanth Venkateswara, Jose Eusebio, Shayok Chakraborty, and Sethuraman Panchanathan. Deep hashing network for unsupervised domain adaptation. In *CVPR*, 2017. [14](#)
- [35] Dequan Wang, Evan Shelhamer, Shaoteng Liu, Bruno Olshausen, and Trevor Darrell. Tent: Fully test-time adaptation by entropy minimization. In *ICLR*, 2020. [2](#), [3](#), [6](#), [14](#)
- [36] Tianyunxi Wei, Yijin Huang, Li Lin, Pujin Cheng, Sirui Li, and Xiaoying Tang. Saliency-guided and patch-based mixup for long-tailed skin cancer image classification. *arXiv:2406.10801*, 2024. [3](#)
- [37] Zhan Wu, Gonglei Shi, Yang Chen, Fei Shi, Xinjian Chen, Gouenou Coatrieux, Jian Yang, Limin Luo, and Shuo Li. Coarse-to-fine classification for diabetic retinopathy grading using convolutional neural network. *Artificial Intelligence in Medicine*, 108:101936, 2020. [1](#)
- [38] Tongkun Xu, Weihua Chen, WANG Pichao, Fan Wang, Hao Li, and Rong Jin. Cdtrans: Cross-domain transformer for unsupervised domain adaptation. In *ICLR*, 2021. [5](#)
- [39] Shiqi Yang, Joost van de Weijer, Luis Herranz, Shangling Jui, et al. Exploiting the intrinsic neighborhood structure for source-free domain adaptation. In *NeurIPS*, 2021. [3](#), [5](#), [6](#)
- [40] Hongxu Yin, Arun Mallya, Arash Vahdat, Jose M Alvarez, Jan Kautz, and Pavlo Molchanov. See through gradients: Image batch recovery via gradinversion. In *CVPR*, 2021. [2](#)
- [41] Chenrui Zhang, Tao Lei, and Ping Chen. Diabetic retinopathy grading by a source-free transfer learning approach. *Biomedical Signal Processing and Control*, 73:103423, 2022. [2](#)

Domain Adaptive Diabetic Retinopathy Grading with Model Absence and Flowing Data

Supplementary Material

7. Reproducibility Statement

The code and data will be made available after the publication of this paper.

8. Proof of Theorem

8.1. A Proof of Theorem 1

Recalling traditional unadversarial learning. Unadversarial learning aims to develop an image perturbation that enhances the performance on a specific class, which can be succinctly described as follows:

$$\hat{\delta} = \arg \min_{\delta} L(f_{\theta}(x + \delta), y), s.t. \|\delta\| \leq \epsilon \quad (9)$$

where $L(\cdot)$ denotes objective function, x and y are input image and its label, f_{θ} is a pre-trained model with parameters θ , δ is a perturbation, ϵ is a small threshold. Solves this problem in an iterative way formulated as

$$\delta_{k+1} = \delta_k + \alpha \cdot \text{sign}(\nabla_x L(f_{\theta}(x + \delta_k), y)), k \in [0, K-1], \quad (10)$$

where α is a trade-off parameter, K is iteration number, δ_0 is an initial random noise. We re-consider the iterative optimization process above and obtain the theorem below.

Restatement of Theorem 1 *Given the unadversarial learning problem defined in Eq. (9), the iterative process featured by Eq. (10) can be expressed as the following generative form.*

$$\delta_k = \delta_0 + V \cdot F_{\Phi} \left(\frac{\partial \delta_0}{\partial x} \right), \quad (11)$$

where δ_0 is an initial random noise, V is a bound constant, F_{Φ} is a generative function.

Proof. First, according to the chain principle, we can convert Eq. (10) into

$$\delta_{k+1} = \delta_k + \alpha \cdot \left(\frac{\partial L}{\partial f_{\theta}} \cdot \frac{\partial f_{\theta}}{\partial x} \cdot \left(1 + \frac{\partial \delta_k}{\partial x} \right) \right). \quad (12)$$

Since that the learning will converge to the unadversarial examples, $\alpha \cdot \frac{\partial L}{\partial f_{\theta}} \cdot \frac{\partial f_{\theta}}{\partial x}$ is bounded by a certain constant, denoted by $U_k > 0$, thereby Eq. (12) become

$$\delta_{k+1} \leq \delta_k + U_k \left(1 + \frac{\partial \delta_k}{\partial x} \right). \quad (13)$$

We make a further substitution on δ_k according to the law presented in Eq. (13), leading to

$$\delta_{k+1} \leq \left[\delta_{k-1} + U_{k-1} \left(1 + \frac{\partial \delta_{k-1}}{\partial x} \right) \right] + U_k \left(1 + \frac{\partial \delta_k}{\partial x} \right). \quad (14)$$

By continuing this substitution on $\delta_{k-1}, \dots, \delta_0$ in order, we have

$$\begin{aligned} \delta_{k+1} &\leq \delta_0 + U_0 \left(1 + \frac{\partial \delta_0}{\partial x} \right) + U_1 \left(1 + \frac{\partial \delta_1}{\partial x} \right) \\ &\quad + \dots + U_i \left(1 + \frac{\partial \delta_i}{\partial x} \right) + \dots + U_k \left(1 + \frac{\partial \delta_k}{\partial x} \right) \\ &\leq \delta_0 + U_m \left[k + \frac{\partial \delta_0}{\partial x} + \frac{\partial \delta_1}{\partial x} + \dots + \frac{\partial \delta_k}{\partial x} \right], \end{aligned} \quad (15)$$

where $U_m = \max\{U_0, U_1, \dots, U_k\}$.

To obtain generative form, we explore the relationships between $\{\frac{\partial \delta_1}{\partial x}, \frac{\partial \delta_2}{\partial x}, \dots, \frac{\partial \delta_k}{\partial x}\}$ and $\frac{\partial \delta_0}{\partial x}$, respectively. To this end, we first investigate the relationship between $\frac{\partial \delta_1}{\partial x}$ and $\frac{\partial \delta_0}{\partial x}$, combining Eq. (13).

$$\frac{\partial \delta_1}{\partial x} \leq \frac{\partial \delta_0}{\partial x} + U_1 \cdot \frac{\partial}{\partial x} \left(\frac{\partial \delta_0}{\partial x} \right) = h_1 \left(\frac{\partial \delta_0}{\partial x} \right) \quad (16)$$

where, $h_1(\cdot)$ stands for an equivalent function. For $\frac{\partial \delta_2}{\partial x}$, we have the following equation based on Eq. (13) and Eq. (16).

$$\begin{aligned} \frac{\partial \delta_2}{\partial x} &\leq \frac{\partial \delta_1}{\partial x} + U_2 \cdot \frac{\partial}{\partial x} \left(\frac{\partial \delta_1}{\partial x} \right) \\ &= h_1 \left(\frac{\partial \delta_0}{\partial x} \right) + U_2 \cdot \frac{\partial}{\partial x} \left(h_1 \left(\frac{\partial \delta_0}{\partial x} \right) \right) \\ &= h_2 \left(\frac{\partial \delta_0}{\partial x} \right) \end{aligned} \quad (17)$$

In the recursion way presented by Eq. (16) and Eq. (17), $\{\frac{\partial \delta_3}{\partial x}, \dots, \frac{\partial \delta_k}{\partial x}\}$ can be expressed as

$$\frac{\partial \delta_3}{\partial x} \leq h_3 \left(\frac{\partial \delta_0}{\partial x} \right), \dots, \frac{\partial \delta_k}{\partial x} \leq h_k \left(\frac{\partial \delta_0}{\partial x} \right) \quad (18)$$

Therefore, substituting Eq. (16), (17) and (18) into Eq. (15), we have

$$\delta_{k+1} \leq \delta_0 + U_m \left[k + \frac{\partial \delta_0}{\partial x} + h_1 \left(\frac{\partial \delta_0}{\partial x} \right) + \dots + h_k \left(\frac{\partial \delta_0}{\partial x} \right) \right]. \quad (19)$$

Let $F_{\Phi} \left(\frac{\partial \delta_0}{\partial x} \right) = \left[k + \frac{\partial \delta_0}{\partial x} + h_1 \left(\frac{\partial \delta_0}{\partial x} \right) + \dots + h_k \left(\frac{\partial \delta_0}{\partial x} \right) \right]$ and V be a value that makes the equality relationship hold. Eq. (19) becomes the generative form below.

$$\delta_k = \delta_0 + V \cdot F_{\Phi} \left(\frac{\partial \delta_0}{\partial x} \right). \quad (20)$$

8.2. A Proof of Theorem 2

Recalling the calculation of the fine-grained saliency map. It calculates saliency by measuring central-surround differences within images.

$$G(h, w) = \sum_{\varsigma} \max \{ \text{cen}(h, w) - \text{sur}(h, w, \varsigma), 0 \},$$

$$\text{cen}(h, w) = I(h, w),$$

$$\text{sur}(h, w, \varsigma) = \frac{\sum_{h'=-\varsigma}^{h'=\varsigma} \sum_{w'=-\varsigma}^{w'=\varsigma} I(h+h', w+w') - I(h, w)}{(2\varsigma+1)^2 - 1}, \quad (21)$$

where (h, w) is the coordinate of one pixel in grey-scale image (transformed by x_t) with its corresponding value denoted as $I(w, h)$, and $\varsigma \in \{1, 3, 7\}$ denotes surrounding values.

Restatement of Theorem 2 *Given the partial derivatives of the initial random noise δ_0 w.r.t image x is $\frac{\partial \delta_0}{\partial x}$ and x 's saliency map is $s = G(x)$ where G is the computation function of saliency map. We have the following relationship:*

$$\frac{\partial \delta_0}{\partial x} \leq U \cdot s, \quad (22)$$

where $U > 0$ is a bound constant.

Proof. we treat s as a middle variable, thus $\frac{\partial \delta_0}{\partial x}$ can be expressed as the following equation by the chain law.

$$\frac{\partial \delta_0}{\partial x} = \frac{\partial \delta_0}{\partial s} \cdot \frac{\partial s}{\partial x} \leq U \cdot \frac{\partial s}{\partial x}, \quad (23)$$

where $U > 0$ is a bound constant. In Eq. (23), the inequality holds because both the initial noise and the specific saliency map are bounded, resulting in the relative changes between them also being restricted. In addition, according to the definition of derivative, we have

$$\frac{\partial s}{\partial x} = \frac{\partial G(x)}{\partial x} \approx \frac{G(x + \Delta_x) - G(x)}{\Delta_x}, \quad (24)$$

where Δ_x is a tiny variation.

It is known that the saliency map at (h, w) is only related to itself and its surrounding pixels. Without loss of generality, we build the proof based on the simplest surround case $\varsigma = 1$ where Δ_x at (h, w) is presented by Fig. 9. According to Eq. (21), we have

$$\begin{aligned} \text{cen}(h, w, \Delta_x) &= \text{cen}(h, w) + I_{\Delta} = I_{hw} + I_{\Delta}. \\ \text{sur}(h, w, \varsigma, \Delta_x) &= \frac{\sum_{i=1}^4 (I_i + I_{\Delta i}) - (I_{hw} + I_{\Delta})}{8}, \\ &= \frac{(\sum_{i=1}^4 I_i - I_{hw}) + (\sum_{i=1}^4 I_{\Delta i} - I_{\Delta})}{8}, \\ &= \frac{\text{sur}(h, w, \varsigma) + \text{sur}_{\Delta}(\varsigma, \Delta_x)}{8}. \end{aligned} \quad (25)$$

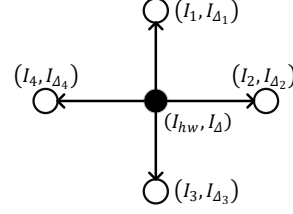


Figure 9. Illustration of $x + \Delta_x$ at coordinate (h, w) as we select the simplest surround case $\varsigma = 1$.

Thus, $G(x + \Delta_x)$ at (h, w) can be expressed as

$$G_{hw}(x + \Delta_x) = \sum_{\varsigma} \max \left\{ \left[\text{cen}(h, w) - \frac{1}{8} \text{sur}(h, w, \varsigma) \right] - \left[\frac{1}{8} \text{sur}_{\Delta}(\varsigma, \Delta_x) - I_{\Delta} \right], 0 \right\} \quad (26)$$

Let $A_1 = \text{cen}(h, w)$ and $A_2 = \text{sur}(h, w, \varsigma)$, $B_1 = \text{cen}(h, w) - \frac{1}{8} \text{sur}(h, w, \varsigma)$, $B_2 = \frac{1}{8} \text{sur}_{\Delta}(\varsigma, \Delta_x) - I_{\Delta}$. Eq. (24) has two situations as follows.

- S-1. When $A_1 > A_2, B_1 > B_2$ or $A_1 < A_2, B_1 > B_2$,

$$\begin{aligned} &\frac{G(x + \Delta_x) - G(x)}{\Delta_x} \\ &= \frac{I_{\Delta} - \frac{1}{8} \text{sur}_{\Delta}(\varsigma, \Delta_x)}{I_{\Delta}} \\ &= \frac{1}{2} - \sum_{i=1}^4 \frac{I_{\Delta i}}{I_{\Delta}} \end{aligned} \quad (27)$$

- S-2. When $A_1 > A_2, B_1 < B_2$ or $A_1 < A_2, B_1 < B_2$,

$$\frac{G(x + \Delta_x) - G(x)}{\Delta_x} = 0 \quad (28)$$

The results presented above suggest a insight that $\frac{\partial s}{\partial x}$ is proportional to the saliency map s , namely

$$\frac{\partial s}{\partial x} \propto s. \quad (29)$$

There are two reasons contributing to this conclusion. First, $\frac{\partial s}{\partial x}$ values confine to a binary situation. More importantly, as shown in Eq. (27), $\frac{\partial s}{\partial x}$ describes the relative change relationship between the current pixel and its surrounding pixels. Combing Eq. (23) and Eq. (29), we have

$$\frac{\partial \delta_0}{\partial x} \leq U \cdot \frac{\partial s}{\partial x} \propto U \cdot s. \quad (30)$$

9. Implementation Details

9.1. Datasets Details

Dataset description. We evaluate the proposed method on four standard DR benchmarks. Their details are presented as follows.

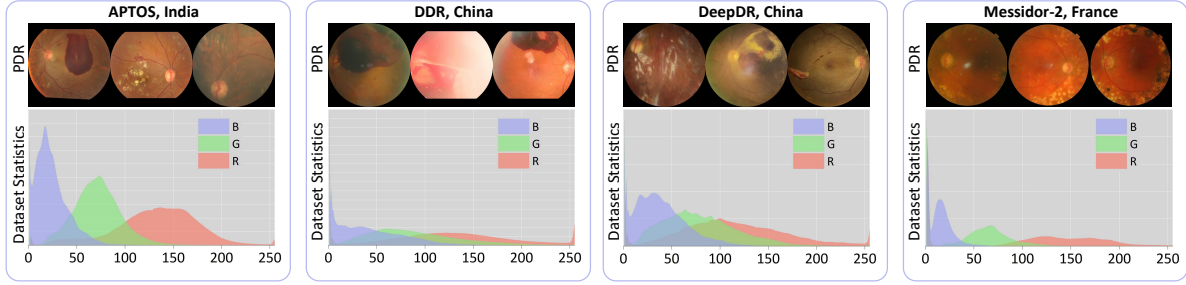


Figure 10. Visualize the styles and characteristics of each dataset by analyzing the RGB statistics of proliferative diabetic retinopathy (PDR) samples across APTOS, DDR, DeepDR, and Messidor-2.

Table 4. Label distribution of the four evaluation datasets: **APTOS**, **DDR**, **DeepDR**, and **Messidor-2**.

Dataset	No DR	Mild DR	Moderate DR	Severe DR	Proliferative DR	Total
APTOS	1,805	370	999	193	295	3,662
DDR	6,265	630	4,477	236	913	13,673
DeepDR	914	222	398	354	112	2,000
Messidor-2	1,017	270	347	75	35	1,748

- **APTOS**. [1] The dataset originates from Kaggle’s APTOS 2019 Blindness Detection Contest, organized by the Asia Pacific Tele-Ophthalmology Society (APTOS). It comprises a total of 5,590 fundus images provided by Aravind Eye Hospital in India. However, only the annotations for the training set (3,662 images) are publicly accessible, and these are used in this study.
- **DDR** [13] The DDR dataset comprises 13,673 fundus images collected from 9,598 patients across 23 provinces in China. These images are classified by seven graders based on features such as soft exudates, hard exudates, and hemorrhages.
- **DeepDR** [17] The DeepDR dataset comprises 2,000 fundus images of both left and right eyes from 500 patients in Shanghai, China.
- **Messidor-2** [7] The Messidor-2 dataset includes 1,748 macula-centered eye fundus images. This dataset partially originates from the Messidor program partners, with additional images contributed by Brest University Hospital in France.

The label distribution of datasets. All datasets exhibit imbalanced class distributions, as shown in Table 4. Specifically, in APTOS, the “No DR” class comprises about **49.2%** of all samples. In DDR, “No DR” accounts for approximately **45.8%**, while in DeepDR, it makes up around **45.7%**. In Messidor-2, the “No DR” class represents about **58.2%** of the total data.

The domain shift of datasets. Each dataset is treated as a distinct domain, with significant variations from factors like country of origin, patient demographics, and differences

in imaging equipment used for acquisition. Additionally, analysis of the RGB statistics for proliferative DR (PDR) samples across these datasets/domains reveals distinct fluctuations in each channel (R, G, and B), highlighting the unique visual styles and characteristics of each dataset, as shown in Fig. 10.

10. Evaluation metrics.

The computation rules for accuracy (termed ACC), Quadratic Weighted Kappa (termed QWK), and the average of QWK and ACC (termed AVG) are as follows.

$$\begin{aligned}
 ACC &= \frac{TP + TN}{TP + TN + FP + FN}, \\
 QWK &= 1 - \frac{\sum_{i=1}^n \sum_{j=1}^n W(i, j) \cdot O(i, j)}{\sum_{i=1}^n \sum_{j=1}^n W(i, j) \cdot E(i, j)}, W_{i,j} = \frac{(i - j)^2}{(C - 1)^2} \\
 AVG &= \frac{1}{2} (ACC + QWK),
 \end{aligned} \tag{31}$$

where TP , TN , FP , and FN represent true positives, true negatives, false positives, and false negatives, respectively. i is a true category, j is a predicted category, C is the number of classes, and n is the total number of samples. $O(i, j)$ is the observed frequency, which represents how many times the true category i was predicted as category j , and $E(i, j)$ is the expected frequency, which indicates how many times category i would be predicted as category j under random guessing, $E(i, j) = P(i) \times P(j) \times n$.

11. Supplementary Experiment Results

11.1. Results with Varying Batch Size

As a supplement to the results with varying batch sizes, Table 5 presents the complete performance of three evaluation metrics across all 12 tasks. TTA methods SHOT-IM and TENT show a performance drop when the batch size is small. Specifically, SHOT-IM decreases by approximately **14.1%** in ACC, **3.9%** in QWK, and **9.1%** when comparing batch sizes of 2 and 64. TENT decreases by approximately **3.0%**

Table 5. Performance of test time adaptation methods evaluated in ACC, QWK, and AVG across different batch sizes

Method	ACC							QWK							AVG						
Source	53.9							60.1							57.0						
	Test Time Adaptation Batch Size							Test Time Adaptation Batch Size							Test Time Adaptation Batch Size						
	2	4	8	16	32	64	Avg.	2	4	8	16	32	64	Avg.	2	4	8	16	32	64	Avg.
SHOT-IM [15]	44.9	54.2	58.5	58.0	59.2	59.0	55.6	60.8	60.9	62.0	63.2	64.4	64.7	62.7	52.8	57.5	60.0	60.8	61.8	61.9	59.1
TENT [35]	56.3	57.1	57.8	58.8	59.7	59.3	58.2	25.1	30.2	39.7	47.2	54.1	59.2	42.6	40.7	43.6	48.7	53.0	56.9	59.3	50.4
SHOT-IM+GUES	60.0	60.9	61.4	61.5	61.4	62.0	61.2	64.7	65.2	65.6	65.8	66.1	66.9	65.7	62.4	63.1	63.5	63.6	63.7	64.5	63.5
TENT+GUES	60.6	61.0	61.3	61.2	61.1	61.0	61.0	62.5	62.3	62.2	62.4	62.5	63.3	62.5	61.5	61.7	61.8	61.8	61.8	62.2	61.8

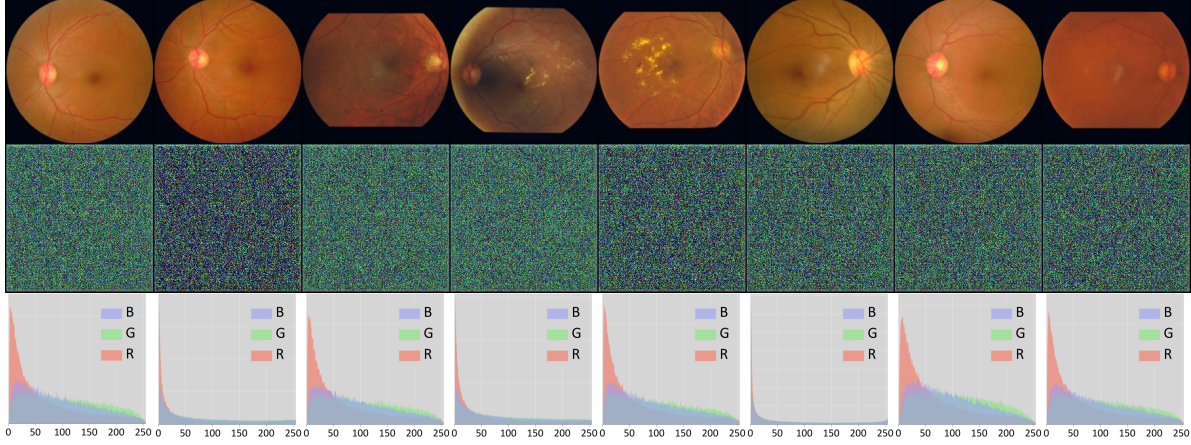


Figure 11. Visualization for input images, generative perturbations, and RGB statistic of the corresponding perturbations on transfer task DDR→APTOS.

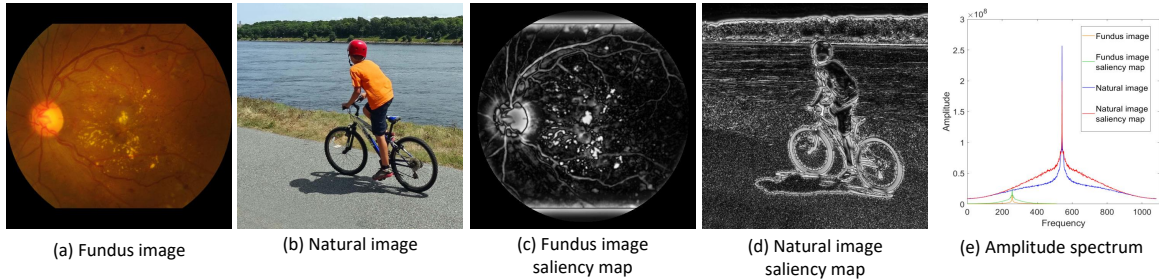


Figure 12. Visualization of a fundus image, a natural image, and their corresponding saliency maps. The fundus image is sampled from APTOS, and the natural image is sampled from Office-Home [34]. In (e), the amplitude spectrum of these four images is displayed.

in ACC, **34.1%** in QWK, and **18.6%** when comparing batch sizes of 2 and 64. However, when these methods are combined with our proposed method, GUES, the decline is not as significant. In SHOT-IM+GUES, the performance shows a decrease of only **2.0%** in ACC, **2.0%** in QWK, and **2.1%** in AVG. In TENT+GUES, the performance shows a decrease of only **0.4%** in ACC, **0.8%** in QWK, and **0.7%** in AVG. These results indicate that our method can prevent declines when the batch size is small, as it predicts individual perturbations that are robust to batch size variations.

11.2. Visualization for Generative Perturbations.

As depicted in Fig. 11, it is evident that different input images exhibit distinct perturbations, as observed directly in the

second row. To be more specific, the RGB distribution of the perturbations, illustrated in the third row, further highlights their variability. This analysis demonstrates how GUES dynamically adjusts the perturbations to account for the unique characteristics of each input image, effectively tailoring them to align with the target domain.

11.3. Why are Saliency Maps Unsuitable for Natural Images?

As we early stated, the proposed method cannot tackle the natural image scenarios well. This part executes a further discussion for this issue using two typical images illustrated in Fig. 12 (a) and (b). There are two key observations to note. First, the fundus image has a simpler background

and structure compared to the natural image, which features richer semantics, including diverse shapes, complex relative structures, and intricate backgrounds. This difference is reflected in the amplitude spectrum in Fig. 12(e), where the fundus image displays a significantly lower frequency band. Second, the saliency maps effectively highlight variations in both fundus and natural images. This is indicated by the fact that the amplitudes of the saliency maps are much larger than the corresponding amplitudes of the images at similar frequencies.

The effects of this enhancement differ between fundus images and natural images. For simpler fundus images, the noticeable variations are typically related to lesions, making the enhancement useful for highlighting these specific regions (see Fig. 12 (c)). In contrast, complex natural images exhibit variations that span the entire scene, such as areas of forest, grass, shadows, and a person riding a bike. In this case, the enhancement draws attention to all elements in the image, which can obscure the factors that are relevant to the task at hand. Therefore, we believe that refining a proper self-supervised signal for natural images represents a promising research direction for the future.